JOURNAL OF GUIDANCE, CONTROL, AND DYNAMICS
Vol. 35, No. 6, November–December 2012

Robust Landing-Guidance Law for Impaired Aircraft

P. K. Menon,* S. S. Vaddi,† and P. Sengupta‡
Optimal Synthesis Inc., Los Altos, California 94022

DOI: 10.2514/1.54213

A guidance law for landing an impaired aircraft is described. The approach involves a planning phase wherein the performance limits of the aircraft are used to design the landing pattern and the reference speed, followed by the guidance computations for generating attitude commands. Commanded attitude can be displayed for the pilot on a heads-up display for manual control, or it can be coupled to the autopilot. Although not detailed in the paper, the guidance law can also generate the flap-deployment schedules and the auto-brake system-initiation trigger in equipped aircraft. Guidance-system development is based on a point-mass, nonlinear model of the aircraft. The feedback-linearization technique is used to transform the system dynamics into a linear, time-invariant form. Finite interval differential-game formulation is then used to derive the robust optimal guidance law. Inverse transformation of the guidance commands to the original coordinate system produces the roll, pitch, and yaw attitude commands. Attitude commands can be tailored for both the crabbed or sideslip flight modes, and for the transitions between them. Simulation results are given to demonstrate the performance and robustness of the proposed approach.

I. Introduction

RECENTLY, there has been significant interest at NASA and other aviation-research centers in making aircraft resilient with respect to performance impairment. Operational experience in the major wars during the twentieth century, in civil air transportation, and in military flight operations over the past three decades has repeatedly demonstrated the capacity of fixed-wing aircraft to survive substantial impairment and continue on to safe landing [1–4]. In most cases, pilot skill has been the key factor in ensuring favorable outcomes. Inspired by such examples, researchers at NASA and other aerospace organizations have been investing resources in developing flight-control systems that will allow impaired aircraft to land successfully. Eventually, these impairment-adaptive, flight-control systems are expected to help compensate for the variations in the human pilot-skill level and contribute toward higher levels of flight safety.

Landing is considered one of the most hazardous phases of an aircraft flight. Even under normal conditions, landing is the highest workload phase of flight operations. During this phase, the pilot is required to reduce the aircraft speed while descending, deploy flaps, extend the landing gear, align the flight path with the runway centerline, and execute the flare or the roundout [5] maneuver. If crosswinds are present, an additional decrab maneuver must be executed at touchdown. Aircraft impairment adds another dimension to this already complex task. By introducing additional uncertainties in the flight envelope, aircraft performance impairment requires the pilot to modify the standard landing procedures under limited information. For instance, flap deployment may need to be delayed or altogether eliminated, and the flare maneuver may need to be steeper than nominal to accommodate for the loss of lift. Moreover, impaired aircraft may not have the option of going around for another landing attempt in case the first attempt fails.

For the present research, it is assumed that inner-loop adaptive stabilization systems such as those described in Refs. [1,2] will ensure that the airframe is returned to a stable flying condition after the impairment. Moreover, it will be assumed that the aircraft flight envelope and maneuver limits can be estimated within a certain error bound using algorithms such as those described in Ref. [6]. The estimated performance models can then be used as the basis for deriving the guidance laws for flare and touchdown. Impairments considered in this paper include the loss of lift from major flying surfaces such as wings and the vertical fin, and partial loss of engine power, including thrust asymmetry.

Typical landing sequence of an aircraft is illustrated in Fig. 1. The major phases of the landing sequences are indicated by waypoints indicated using black hollow circles. Aircraft generally approach the landing area in the downwind direction with an airspeed of approximately 20 kt above the reference speed V_{REF} [5,7] at an altitude of 1500 ft. Note that V_{REF} is 30% higher than the stall speed V_{SO}. This portion of the landing pattern is generally termed as the downwind leg. The flap deployment is initiated when the aircraft is abeam with the runway at approximately its midpoint. The landing gear is deployed when the aircraft is abeam with the expected touchdown point, indicated by the star symbol in Fig. 1. Flap deployment is complete as the aircraft turns into the base leg beginning at waypoint A. The airspeed in the base leg is approximately 10 kt above V_{REF}. The final leg of the landing pattern begins when the flight path is aligned with the runway centerline, denoted by the waypoint B in the figure. The dimensions of the approach pattern depend on aircraft performance capabilities. For instance, the turn to base portion of the approach pattern may be roughly one mile or less for a small general aviation aircraft, but may involve several miles of airspace for a heavy jet aircraft.

During the final leg of the landing pattern, the aircraft flight path is stabilized along the glideslope terminating at a desired aim point on the runway, and its velocity vector is aligned along the runway centerline at approximately 5 kt above V_{REF}. Note that in some cases, the airspace may allow a *straight-in* landing trajectory. In that case, the downwind and base legs will be absent in the pattern, being replaced by a long final leg. The aircraft trajectory must be stabilized by the time it reaches 500 ft altitude, otherwise it is recommended that a go-around maneuver is initiated for another landing attempt. Assuming that the trajectory is stabilized, the aircraft can initiate flare maneuver at approximately 50-ft altitude over the runway threshold to touchdown at approximately 1000 ft down the runway. The flare maneuver decreases the aircraft descent rate to between 100 and 200 ft per minute.

The first phase of the landing guidance law is to determine the dimensions of the approach pattern based on a knowledge of the aircraft performance capabilities, such as turn rate and stall speed.

Presented as Paper 7702 at the AIAA Guidance, Navigation, and Control Conference, Toronto Ontario, August 2–5, 2010; received 10 March 2011; revision received 3 February 2012; accepted for publication 6 February 2012.

*Chief Scientist, 95 First Street, Suite 240. Fellow AIAA.
†Senior Research Scientist, 95 First Street, Suite 240. Member AIAA.
‡Research Scientist, 95 First Street, Suite 240. Senior Member AIAA.

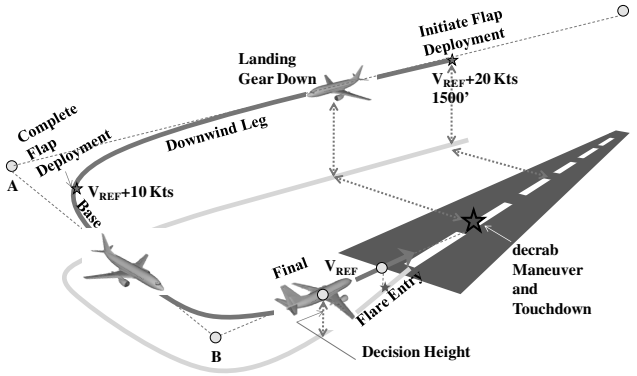

Fig. 1 Typical landing sequence of an aircraft.

These are known under normal conditions, but methods such as discussed in Ref. [6] must be employed in the case of aircraft impairment. The problem of designing the approach pattern on board an impaired aircraft will not be further elaborated in the present paper.

All through the final phase, the aircraft flight path is required to be aligned along the runway centerline. If the crosswinds are minimal, the trajectory can be aligned without difficulty, but if crosswinds are present, the aircraft must adopt either a crabbed-approach path or a sideslip-approach path to continue tracking the runway centerline [4]. Pilots of large aircraft tend to prefer the crabbed approach because it preserves the visual reference with respect to the horizon until the aircraft is close to the runway surface. Note that this maneuver requires use of the rudder to maintain the sideslip while applying the ailerons to counter the roll.

Very close to the touchdown point, a decrabbing maneuver is executed by rolling the aircraft to touchdown on one of the main gears while yawing the aircraft nose to align with the runway centerline and completing the touchdown with the other main gear. The decrab maneuver is carried out simultaneously with the flare. Because both of these maneuvers involve large attitude gyrations close to the ground, extreme care must be exercised to ensure that the airframe does not contact the ground at any point other than at the landing gear. Several example videos illustrating the difficulty of landing in severe crosswinds are available on the worldwide web. The flare maneuver can be challenging even under ideal conditions, and the decrab maneuver during the touchdown in crosswinds adds to the complexity of the task, sometimes requiring a go-around in severe crosswind situations.

The complexity of the flare and decrab maneuvers is largely due to the need to simultaneously satisfy multiple requirements on the flight-control system along the path and at the final touchdown point. For instance, the angle of attack must be precisely controlled to ensure a small negative vertical velocity at touchdown to prevent ballooning and bouncing. The forward speed must be maintained to ensure that sufficient lift is available until the wheels touch down, and then rapidly decreased to minimize floating caused by the ground effect. The crab angle must be maintained to align the aircraft velocity vector along the runway centerline until close to the ground, at which time the aircraft must be rolled to ensure that only one of the main landing gears touches the runway surface before the aircraft nose is aligned along the runway centerline. Immediately after this has occurred, the aircraft must be gently rolled back to allow the other landing gear to touch down while simultaneously yawing to align the aircraft nose with the runway centerline. If it appears that any of these actions may not lead to a successful landing, the aircraft must immediately execute the go-around procedure by increasing the thrust to takeoff setting, retracting the flaps and the landing gear during the climb out.

Alternately, if the main gears have touched down with the nose pointing in the right direction, the aircraft nose must be maintained high enough to rapidly bleed off the airspeed to allow the nose gear to touch down. Reverse thrust and spoilers can then be applied to bring the speed down to a point where the aircraft wheel brakes can be safely applied, completing the landing maneuver. Several books on flight-control system design discuss the flare-control problem [8,9], but none have addressed the simultaneous execution of flare and decrab maneuvers in the presence of uncertainties. Interestingly, the complexities of the flare maneuver motivated one of the early attempts at employing neural networks [10] for designing an adaptive control law for this maneuver. Schaefer [11] developed functional requirements for a B757/B767 autoland system. Shakarian [12] used Monte Carlo techniques to assess the dispersion performance of a B757/B767 autoland system. Wagner et al. [13] designed digital control laws for autolanding using quantitative feedback-control theory. Shue et al. [14] designed robust control laws for glideslope capture under windshear using H_∞ technique. Fuzzy logic-based techniques were used by Nho and Agarwal [15,16] for design of glideslope capture and autoland systems. Heffley [17] conducted closed-loop analysis of the flare maneuver using linear models that were derived from manual landings of real and simulated aircraft. Arents et al. [18] and Ngoc et al. [19] studied the impact of synthetic vision on landing guidance and the flare maneuver. Prasad and Pradeep [20] used the technique of feedback linearization for developing an autolanding system for a fighter aircraft. Kluver [21,22] developed landing-guidance laws for unpowered aircraft using trajectory planning. Kim et al. [23] developed a glidepath-tracking algorithm for autolanding of an unmanned aerial vehicle.

The current work develops a nonlinear, closed-form analytic three-dimensional (3-D) landing-guidance law suitable for onboard implementation. It considers all the key phases of landing, including stabilized approach, flare, and decrab maneuvers. The guidance law is demonstrated on a realistic commercial aircraft model obtained from NASA. Simulation scenarios include both landing-under-crosswind and symmetric loss-of-lift conditions. Asymmetric loss of lift is dynamically equivalent to the crabbed crosswind-landing scenario. Robustness of the guidance law is demonstrated in Monte Carlo simulations, and comparison with a nonlinear numerical optimization-based guidance solution is given.

The following sections will first discuss the aircraft models used in the guidance-law development, followed by the guidance-law derivation and simulation assessment. Near optimality of the proposed approach will be illustrated by comparing its performance with those from a nonlinear programming-based trajectory optimization. Finally, the robustness of the guidance law will be demonstrated through Monte Carlo simulations.

II. Aircraft Models

Rigid-body dynamics of the aircraft model are often used for autopilot design, but point-mass models are more appropriate for use in guidance-law development due to their close connection with aircraft performance parameters. The following subsections will discuss two models used in the present work. The first model is used for guidance-law derivation, whereas the second model is used for simulation evaluation of the guidance law.

A. Point-Mass Dynamics

The point-mass model is defined with respect to a runway-fixed coordinate system shown in Fig. 2. The equations of motion with the assumption of thrust acting along the velocity vector are:

$$\dot{x} = V\cos\gamma\cos\chi \tag{1}$$

$$\dot{y} = V\cos\gamma\sin\chi \tag{2}$$

$$\dot{h} = V\sin\gamma \tag{3}$$

$$\dot{V} = \frac{T-D}{m} - g\sin\gamma \tag{4}$$

$$\dot{\gamma} = \frac{g}{V}\left(\frac{L_h}{W} - \cos\gamma\right) \tag{5}$$

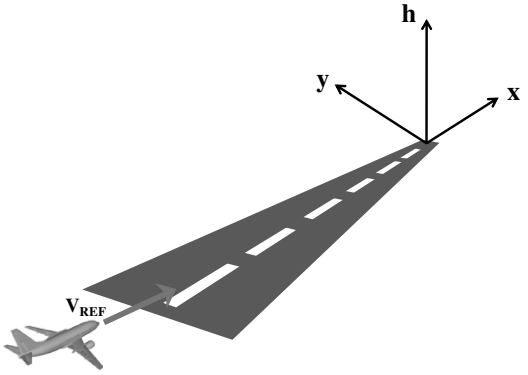

Fig. 2 Coordinate system for point-mass model.

$$\dot{\chi} = \frac{L_y}{mV\cos\gamma} \tag{6}$$

In these equations, T is the thrust, m is the mass, V is the speed, γ is the flight-path angle, χ is the heading angle, L_h and L_y are the aerodynamic forces normal to the velocity vector, and D is the aerodynamic drag. The point-mass model is derived with the assumption that the aircraft is continuously maintained in moment equilibrium using the control surfaces. Thus, the vehicle attitude dynamics are treated as algebraic, and the attitudes are considered to be the control variables.

Note that the forces L_h and L_y can be expressed in terms of lift, and the bank angle can be expressed in bank-to-turn (zero-slip) maneuvers, or in terms of lift and side force for skid-to-turn maneuvers. The lift and side-force components can be expressed in terms of angle of attack and angle of sideslip. Given the orientation of the velocity vector in the inertial frame through the flight-path angle γ and the heading angle χ, the pitch-yaw-roll body attitudes necessary to generate a desired angle of attack and the angle of sideslip can be computed. These angles can be used for pilot guidance or they can be directly coupled to the attitude-tracking autopilot.

B. Simulation Model

In addition to the point-mass dynamics, the simulation model captures the autopilot-attitude dynamics through linear second-order dynamic systems defined along each axis. Note that this representation of the attitude-tracking autopilot dynamics will be exact if its design is based on the feedback linearization methodology. The point-mass equations of motion of the aircraft in an earth-fixed inertial frame are given by:

$$\begin{bmatrix} m\ddot{X} \\ m\ddot{Y} \\ m\ddot{Z} \end{bmatrix} = \begin{bmatrix} c_\theta c_\psi & s_\phi s_\theta c_\psi - c_\phi s_\psi & c_\phi s_\theta c_\psi + s_\phi s_\psi \\ c_\theta s_\psi & s_\phi s_\theta s_\psi + c_\phi c_\psi & c_\phi s_\theta s_\psi - s_\phi c_\psi \\ -s_\theta & s_\phi c_\theta & c_\phi c_\theta \end{bmatrix} \times \begin{bmatrix} T - \frac{1}{2}\rho V^2 S_{\text{ref}} C_x(\alpha,\beta) \\ \frac{1}{2}\rho V^2 S_{\text{ref}} C_y(\alpha,\beta) \\ \frac{1}{2}\rho V^2 S_{\text{ref}} C_z(\alpha,\beta) \end{bmatrix} + \begin{bmatrix} 0 \\ 0 \\ mg \end{bmatrix} \tag{7}$$

Note that the sine and cosine functions in the transformation matrix in Eq. (7) have been abbreviated for the sake of compactness. The control variables in this model are the aircraft attitude components acting through the angle-of-attack/angle-of-sideslip variables and thrust. The autopilot is modeled as three decoupled second-order dynamic systems, and the engine dynamics are modeled as a first-order system given by following equations:

$$\begin{aligned} \ddot{\phi} &= -k_{p1}(\phi - \phi_{\text{command}}) - k_{v1}\dot{\phi} \\ \ddot{\theta} &= -k_{p2}(\theta - \theta_{\text{command}}) - k_{v2}\dot{\theta} \\ \ddot{\psi} &= -k_{p3}(\psi - \psi_{\text{command}}) - k_{v3}\dot{\psi} \end{aligned} \tag{8}$$

$$\dot{T} = -k_{pT}(T - T_{\text{command}}) \tag{9}$$

The variable ρ is the atmospheric density; C_x, C_y, and C_z are the body-axis-referenced aerodynamic force coefficients; S_{ref} is the reference area; ψ, θ, and ϕ are the body attitudes; and T is the thrust. The subscript *command* denotes commanded values. The approximate proportional gains in the autopilot-control loops are k_{p1}, k_{p2}, and k_{p3}; and the derivative gains are denoted by k_{v1}, k_{v2}, and k_{v3}. The engine proportional gain is denoted by k_{pT}.

III. Landing-Guidance Law

Because the point-mass model is nonlinear, it is not readily amenable to the derivation of guidance laws in feedback form using the theory of optimal control [24] and differential games [25]. Following previous research efforts [26–29], the system dynamics can be first transformed into linear, time-invariant form using feedback linearization [30–32]. The guidance problem can then be solved using the transformed dynamics, and then inverse transformed in terms of the original variables. The resulting solution will be in nonlinear-feedback form, suitable for real-time implementation as outlined in the following sections.

A. Feedback Linearization of the Aircraft Point-Mass Dynamics

The first step in the transformation involves the differentiation of the kinematic Eqs. (1–3), followed by the substitutions from Eqs. (4–6) to yield:

$$\ddot{x} = \frac{(T-D)}{m}\cos\gamma\cos\chi - \frac{L_h\sin\gamma\cos\chi}{m} - \frac{L_y\sin\chi}{m} \tag{10}$$

$$\ddot{y} = \frac{(T-D)}{m}\cos\gamma\sin\chi - \frac{L_h\sin\gamma\sin\chi}{m} + \frac{L_y\cos\chi}{m} \tag{11}$$

$$\ddot{h} = \frac{(T-D)}{m}\sin\gamma + \frac{L_h\cos\gamma}{m} - g \tag{12}$$

Expressions (10–12) describe the aircraft point-mass dynamics in the inertial frame. The transcendental functions given in terms of the flight-path angle and the heading angle on the right-hand sides of these equations can be computed from the inertial velocity components as:

$$\sin\gamma = \frac{\dot{h}}{\sqrt{\dot{h}^2 + \dot{x}^2 + \dot{y}^2}} \qquad \cos\gamma = \pm\frac{\sqrt{\dot{x}^2 + \dot{y}^2}}{\sqrt{\dot{h}^2 + \dot{x}^2 + \dot{y}^2}} \tag{13}$$

$$\sin\chi = \frac{\dot{y}}{\sqrt{\dot{x}^2 + \dot{y}^2}} \qquad \cos\chi = \frac{\dot{x}}{\sqrt{\dot{x}^2 + \dot{y}^2}} \tag{14}$$

Because the aerodynamic forces on the aircraft are based on its relative speed with respect to the atmosphere, the transformation of the horizontal- and vertical-lift components to the aircraft attitudes must be carried out with respect to the relative velocity vector. For this purpose, the components of the wind-velocity vector are assumed to be specified in the same X-Y-H coordinate system as the equations of motion. The airspeed is then given by:

$$V_a = \sqrt{(\dot{x} - \dot{x}_w)^2 + (\dot{y} - \dot{y}_w)^2 + (\dot{h} - \dot{h}_w)^2} \tag{15}$$

The flight-path angle and the heading angle of the airspeed vector can be computed as:

$$\sin\gamma_w = \frac{\dot{h}-\dot{h}_w}{\sqrt{(\dot{x}-\dot{x}_w)^2+(\dot{y}-\dot{y}_w)^2+(\dot{h}-\dot{h}_w)^2}}$$
$$\cos\gamma_w = \pm\frac{\sqrt{(\dot{x}-\dot{x}_w)^2+(\dot{y}-\dot{y}_w)^2}}{\sqrt{(\dot{x}-\dot{x}_w)^2+(\dot{y}-\dot{y}_w)^2+(\dot{h}-\dot{h}_w)^2}} \tag{16}$$

$$\sin\chi_w = \frac{\dot{y}-\dot{y}_w}{\sqrt{(\dot{x}-\dot{x}_w)^2+(\dot{y}-\dot{y}_w)^2}}$$
$$\cos\chi_w = \frac{\dot{x}-\dot{x}_w}{\sqrt{(\dot{x}-\dot{x}_w)^2+(\dot{y}-\dot{y}_w)^2}} \tag{17}$$

The equations of motion can then be recast in terms of the atmosphere-relative velocity vector to yield:

$$\ddot{x} = \frac{(T-D)}{m}\cos\gamma_w\cos\chi_w - \frac{L_{hw}\sin\gamma_w\cos\chi_w}{m} - \frac{L_{yh}\sin\chi_w}{m} = U_x \tag{18}$$

$$\ddot{y} = \frac{(T-D)}{m}\cos\gamma_w\sin\chi_w - \frac{L_{hw}\sin\gamma_w\sin\chi_w}{m} + \frac{L_{yw}\cos\chi_w}{m} = U_y \tag{19}$$

$$\ddot{h} = \frac{(T-D)}{m}\sin\gamma_w + \frac{L_{hw}\cos\gamma_w}{m} - g = U_h \tag{20}$$

The right-hand sides of Eqs. (18–20) are next denoted by pseudo-control variables U_x, U_y, and U_z to define the transformed dynamics of the aircraft. Note that the system is in linear, time-invariant, and decoupled form in terms of the pseudo-control variables. The state variables in the transformed model are the position and velocity components of the aircraft in the inertial frame. The pseudo-control variables are the acceleration components in the inertial frame.

The pseudo-control variables can be inverse transformed to thrust, pitch, yaw, and roll attitude using algebraic transformations, as illustrated in Sec. III.E. An available degree of freedom in this transformation is the fact that the aircraft can be operated in bank-to-turn or skid-to-turn modes. Pitch-yaw attitudes at arbitrary roll attitudes can be used to create skid-to-turn maneuvers such as the crabbed approach, whereas specific pitch-yaw-roll attitudes can be used to create bank-to-turn maneuvers useful for sideslip approaches.

It is reasonable to assume that minor changes to aircraft thrust will be made by the auto-throttle or the pilot to keep the speed essentially constant during the descent. Consequently, the thrust magnitude can be assumed to be equal to drag.

Because the transformed point-mass dynamics are linear and time invariant with respect to the pseudo-control variables, linear optimal-control and differential-game theories can be directly applied to this guidance problem, as illustrated in the following section.

B. Robust Finite Interval Optimal Guidance

Because the transformed point-mass dynamics of the aircraft form are in decoupled form, the guidance-law derivation will only be illustrated along one the vertical direction. The development for the lateral direction can be carried out in an entirely analogous form. The coupling between the lateral and longitudinal dynamics occurs through the inverse feedback-linearizing transformation.

The feedback-linearized model of the aircraft in the vertical direction can be written as:

$$\ddot{Z} = a - b \tag{21}$$

Here a is acceleration in the vertical direction, and b represents the external disturbance in the same direction. A similar equation can be written for the Y coordinate as well. The objective of the landing-guidance law is to transfer the aircraft from its initial position and velocity to a desired waypoint with a specified velocity at a specified final time while subjecting it to the least amount of acceleration. The guidance law should simultaneously minimize the impact of external disturbances on the trajectories. This can be achieved by minimizing a performance index of the form.

$$J = \left[\frac{1}{2}S_1(Z_f - Z_{f\mathrm{des}})^2 + \frac{1}{2}S_2(\dot{Z}_f - \dot{Z}_{f\mathrm{des}})^2\right]\Big|_{t=t_f} + \frac{1}{2}\int_0^{t_f}(Ra^2 - \varepsilon b^2)\,\mathrm{d}t \tag{22}$$

The first term in the performance index penalizes the deviations in the aircraft position from a specified waypoint location at the specified final time, and the second term penalizes the velocity error. The first term in the integrand imposes the objective of minimizing the acceleration. The second term in the integrand arises from the need to make the guidance law robust with respect to external disturbance b. The negative sign of this term arises from the differential-game view of the disturbances, which assumes that the disturbances always act in such a way as to maximize the performance index.

The parameters S_1, S_2, and R can be chosen to establish relative weighting between the terminal-position error, the velocity error, and the acceleration magnitudes. The variational Hamiltonian for the optimal-control problem, (21) and (22), can be used to derive the co-state equations while enforcing the optimality condition. This process yields:

$$H = \frac{1}{2}(Ra^2 - \varepsilon b^2) + \lambda_1\dot{Z} + \lambda_2(a-b) \tag{23}$$

$$\dot{\lambda}_1 = 0 \qquad \lambda_1 = \lambda_1(0) \tag{24}$$

$$\dot{\lambda}_2 = -\lambda_1 \qquad \lambda_2 = \lambda_2(0) - \lambda_1(0)t \tag{25}$$

Optimality condition [24] can be used to derive the optimal control and worst case disturbance as:

$$a = -\frac{\lambda_2}{R} = -\frac{(\lambda_2(0) - \lambda_1(0)t)}{R} \tag{26}$$

$$b = -\frac{\lambda_2}{\varepsilon} = -\frac{(\lambda_2(0) - \lambda_1(0)t)}{\varepsilon} \tag{27}$$

Boundary conditions on the co-states at the specified final time are given by:

$$\lambda_{1f} = S_1(Z_f - Z_{f\mathrm{des}}) \tag{28}$$

$$\lambda_{2f} = S_2(\dot{Z}_f - \dot{Z}_{f\mathrm{des}}) \tag{29}$$

Substituting the expression for control and worst-case disturbance into the transformed equations of motion and integrating yields the following expressions for acceleration, velocity, and position:

$$\ddot{Z} = -\frac{(\lambda_2(0) - \lambda_1(0)t)}{R} + \frac{(\lambda_2(0) - \lambda_1(0)t)}{\varepsilon} = -(\lambda_2(0) - \lambda_1(0)t)\left(\frac{1}{R} - \frac{1}{\varepsilon}\right) \tag{30}$$

$$Z_f = Z(0) + \dot{Z}(0)t_f - \left(\frac{1}{R} - \frac{1}{\varepsilon}\right)\frac{\lambda_2(0)t_f^2}{2} + \left(\frac{1}{R} - \frac{1}{\varepsilon}\right)\frac{\lambda_1(0)t_f^3}{6} \tag{31}$$

$$\dot{Z}_f = \dot{Z}(0) - \lambda_2(0)t_f\left(\frac{1}{R} - \frac{1}{\varepsilon}\right) + \lambda_1(0)t_f^2\left(\frac{1}{R} - \frac{1}{\varepsilon}\right) \tag{32}$$

Substituting these expressions in the expressions for co-state boundary conditions (28) and (29) yields the following linear system of equations:

$$\begin{bmatrix}\lambda_1(0)\\ \lambda_2(0)\end{bmatrix}=\frac{1}{Det}\begin{bmatrix}-\left(\frac{1}{R}-\frac{1}{\varepsilon}\right)\frac{S_1t_f^2}{2} & \left(\frac{1}{R}-\frac{1}{\varepsilon}\right)S_2t_f+1\\ -\left(\frac{1}{R}-\frac{1}{\varepsilon}\right)\frac{S_1t_f^3}{6}+1 & \left(\frac{1}{R}-\frac{1}{\varepsilon}\right)\frac{S_2t_f^2}{2}+t_f\end{bmatrix}\times\begin{bmatrix}S_2(\dot{Z}_{f\text{des}}-\dot{Z}(0))\\ S_1(Z_{f\text{des}}-Z(0)-\dot{Z}(0)t_f)\end{bmatrix} \tag{33}$$

with

$$Det=\left[\left(-\left(\frac{1}{R}-\frac{1}{\varepsilon}\right)\frac{S_1t_f^2}{2}\right)\left(\left(\frac{1}{R}-\frac{1}{\varepsilon}\right)\frac{S_2t_f^2}{2}+t_f\right)-\left(-\left(\frac{1}{R}-\frac{1}{\varepsilon}\right)\frac{S_1t_f^3}{6}+1\right)\left(\left(\frac{1}{R}-\frac{1}{\varepsilon}\right)S_2t_f+1\right)\right]$$

Given the waypoint locations and the desired speeds at those waypoints, the expression (33) can be solved to yield the initial values of the co-states. These can then be used to compute the control in the vertical direction at the initial time as:

$$a(0)=-\frac{\lambda_2(0)}{R} \tag{34}$$

Following Ref. [24], this control variable can be recast in terms of time-to-go to define the control variable at the initial time given by (34) as the control variable at the present time t.

C. Inverse Transformation

The finite-interval guidance law developed in the previous section computes the acceleration components in the vertical and horizontal directions for landing the aircraft in the presence of disturbances while satisfying waypoint constraints. These acceleration components can be transformed into the body attitude commands for use by the pilot in a heads-up display or for direct tracking by the autopilot. Because this transformation process is complex, it will be carried out in multiple steps in the following section.

Given U_y and U_h, the components of the accelerations normal to the relative velocity vector required to execute the landing trajectory, along with the assumption that $T=D$, the components of the aerodynamic forces normal to the relative velocity vector can be computed from:

$$L_{yw}=-\frac{1}{\cos\chi_w}(mU_y+L_{hw}\sin\gamma_w\sin\chi_w) \tag{35}$$

$$L_{hw}=\frac{m}{\cos\gamma_w}(U_h+g) \tag{36}$$

The next step in the transformation is that of converting the horizontal and vertical forces given by Eqs. (35) and (36) first into aerodynamic coefficients and then into aircraft attitudes. Note that the transformed model involves only the two components of acceleration with respect to the inertial frame. The aircraft attitude, however, has three components: the pitch, yaw, and roll attitudes. Thus, the transformation from the acceleration components into attitudes has a free-degree-of-freedom. This additional degree of freedom can be used to enforce an additional constraint.

During conventional 3-D maneuvers involving aircraft with a vertical plane of symmetry, this constraint is enforced through the *coordinated flight* requirement, which constrains the angle of sideslip to remain zero throughout maneuvers. A second approach is the skid-to-turn maneuver, which explicitly employs an angle of sideslip to generate lateral acceleration. Such maneuvers may occur in impaired aircraft that may not have a vertical plane of symmetry. Skid-to-turn maneuvers may also arise during crabbed flight under crosswind conditions. In fighter aircraft, the skid maneuver is often used for pointing body-fixed weapon systems in a desired direction. Notably, most axisymmetric missiles employ skid-to-turn maneuvers during their normal operation. The following sections discuss transformations to enable both these maneuvers.

D. Skid-to-Turn Mode

The skid-to-turn mode may be employed during the stabilized-approach phase of the landing. In the lateral direction, this mode is characterized by the existence of non-zero angles of sideslip. Pitch and yaw attitudes are used to realize the desired angle of attack and angle of sideslip, with the roll attitude maintained at zero. First, the desired lift and side-force coefficients are computed using the forces given by Eqs. (35) and (36) to yield:

$$C_{L\_\text{desired}}=\frac{L_{hw}}{0.5\rho V_a^2S}\qquad C_{S\_\text{desired}}=\frac{L_{yw}}{0.5\rho V_a^2S} \tag{37}$$

The angle of attack and angle of sideslip corresponding to the desired lift and side-force coefficients can be determined from the tables listing the relationship between angle of attack and lift coefficient, and the angle of sideslip and side force. If these tables are symbolically denoted by the functions f_L and f_S, these computations can be summarized as:

$$\alpha_w=f_L^{-1}(C_{L\_\text{desired}})\qquad \beta_w=f_S^{-1}(C_{S\_\text{desired}}) \tag{38}$$

At small angles of attack and angles of sideslip, these functional relationships are linear, but they can be highly nonlinear if the aircraft is operating at an extreme angle of attack and angle of sideslip. Once the angle of attack and angle of sideslip are computed, the next step in the process is that of computing the corresponding yaw-pitch attitudes or pitch-roll attitudes. For small angles of attack and angles of sideslip, the roll-pitch-yaw attitudes can be expressed as:

$$\phi=0\qquad \theta=\alpha_w+\gamma_w\qquad \psi=-\chi_w-\beta_w \tag{39}$$

E. Bank-to-Turn Mode

The bank-to-turn mode is employed by aircraft under normal aircraft operations. Angle of attack and bank angle are used to realize the desired aerodynamic forces in this mode. Because the angle of sideslip is required to be zero, the side-force coefficients are not used in the computations. The aerodynamic lift and the desired lift coefficient are first computed as:

$$L=\sqrt{L_{hw}^2+L_{yw}^2}\Rightarrow C_{L\_\text{desired}}=\frac{L}{0.5\rho V_a^2S} \tag{40}$$

Next, the angle of attack and bank angle are computed as:

$$\alpha_{Tw}=f_L^{-1}(C_{L\_\text{desired}})\qquad \Phi_w=\tan^{-1}\left(\frac{L_{yw}}{L_{hw}}\right) \tag{41}$$

These controls will yield bank-to-turn or coordinated maneuvers ($\beta=0$). The roll-pitch attitudes for small angles of attack and small bank angles can then be recovered as:

$$\phi=-\Phi_w\qquad \theta=\alpha_{Tw}+\gamma_w \tag{42}$$

The yaw attitude is computed such that ($\beta=0$). Note that the expressions for attitude in terms of the angle of attack and bank angle assume small-angle approximations. The relationships for large angles are a little more involved.

Aircraft operate in either one of the modes during most of their flight, and thus there is a specific maneuver that employs a combination of these modes. This is the terminal decrab maneuver wherein the aircraft nose is intentionally rotated away from the wind direction to point along the runway centerline. This creates an angle of sideslip, requiring the aircraft to bank toward the wind to counter the side force to keep it aligned along the runway centerline.

IV. Closed-Loop Simulation Results

The guidance law discussed in the previous section is evaluated in a simulation. The following parameters extracted from the NASA GTM aircraft model [33] are used in the simulation.

$$m = 198000 \text{ lbs} \qquad S_{\text{ref}} = 1951 \qquad \rho = 0.0075 \text{ slug/ft}^3$$
$$V_{\text{stall}} = 107 \text{ knots} \qquad V_{\text{ref}} = 145 \text{ knots}$$

The following autopilot time-constants from Ref. [9] are used in the roll, pitch, and yaw channels:

$$t_{cr} = 6.3 \text{ s} \qquad t_{cp} = 3.88 \text{ s} \qquad t_{cy} = 6.3 \text{ s}$$

The damping ratios for all three axes are set as $\zeta_r = \zeta_p = \zeta_y = 0.707$.

After several trials, the terminal state-weighting factors, control-weighting factor, and the disturbance-weighing factor for the optimal guidance law are chosen as:

$$S_1 = 1e2 \qquad S_2 = 1e8 \qquad R = 1 \qquad \varepsilon = 2$$

A. Guidance Law Implementation

Only the final leg of the landing pattern consisting of stabilized approach, flare, and decrab are presented in this paper, as they form the most crucial portions of the landing trajectory. Three waypoints are chosen for the final landing phase based on code of federal regulations (CFR) Part 14 [5]. These are 1) stabilized-approach checkpoint, 2) threshold, and 3) the touchdown point. CFR Part 14 recommends the glideslope to be between 2.5 and 3 deg. The glideslope is set to 2.75 deg in the present simulations, with the duration of flare being set to six seconds and the vertical speed at touchdown required to be at 200 ft/ min. Desired states at the three waypoints are specified as:

$$h_1 = 500 \text{ ft}, \qquad \dot{h}_1 = V_{\text{ref}} \sin 2.75^0, \qquad y_1 = 0,$$
$$\dot{y}_1 = 0 \qquad @x_1 = -\frac{500 - 50}{\tan 2.75^0} - L_{rwy} \tag{43}$$

$$h_2 = 50 \text{ ft}, \qquad \dot{h}_2 = V_{\text{ref}} \sin 2.75, \qquad y_2 = 0,$$
$$\dot{y}_2 = 0 \qquad @x_2 = -L_{rwy} \tag{44}$$

$$h_3 = 0, \qquad \dot{h}_3 = 200 \text{ ft/ min}, \qquad y_3 = 0,$$
$$\dot{y}_3 = 0, \qquad @x_3 = V_{\text{ref}} \cos 2.75^0 * t_{\text{flare}} - L_{rwy} \tag{45}$$

These serve as boundary conditions for optimal-guidance law in the final phase. The time-to-go for the guidance law is computed using the equation:

$$t_{2go} = -\frac{\text{range\_2\_waypo int}}{\text{range\_rate}} = -\frac{(x - x_i)^2 + (y - y_i)^2 + (z - z_i)^2}{(x - x_i)\dot{x} + (y - y_i)\dot{y} + (z - z_i)\dot{z}} \tag{46}$$

The aircraft is expected to stay close to the reference speed throughout the final segment of the landing pattern. Thrust required for maintaining constant airspeed is computed by setting the derivative of the airspeed to zero to yield:

$$0 = \dot{V}_a = \frac{1}{V_a}[(\dot{x} - \dot{x}_w) \quad (\dot{y} - \dot{y}_w) \quad (\dot{h} - \dot{h}_w)] \begin{bmatrix} U_x \\ U_y \\ U_h \end{bmatrix} \tag{47}$$

Because U_y and U_h are known from the guidance-law computations, the value of U_x that will ensure constant airspeed can be computed. This value of acceleration, together with the lateral and vertical aerodynamic forces, and the drag can be used to compute the thrust setting that will achieve constant airspeed. This thrust setting is used until the aircraft reaches the stabilized approach check altitude of 500 ft. The thrust is fixed beyond that point.

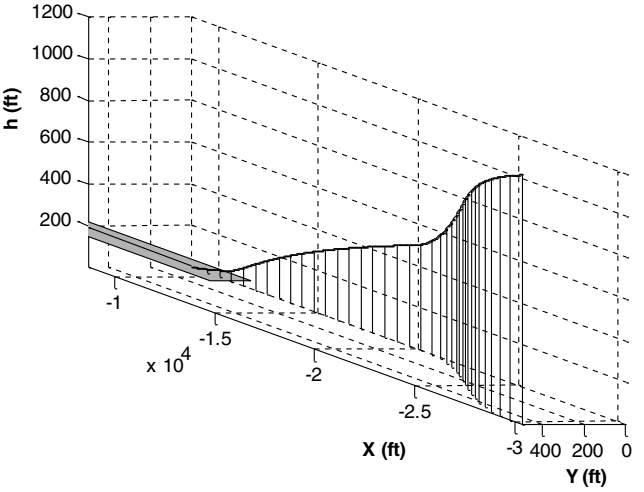

Fig. 3 Final segment of the landing trajectory in three dimensions.

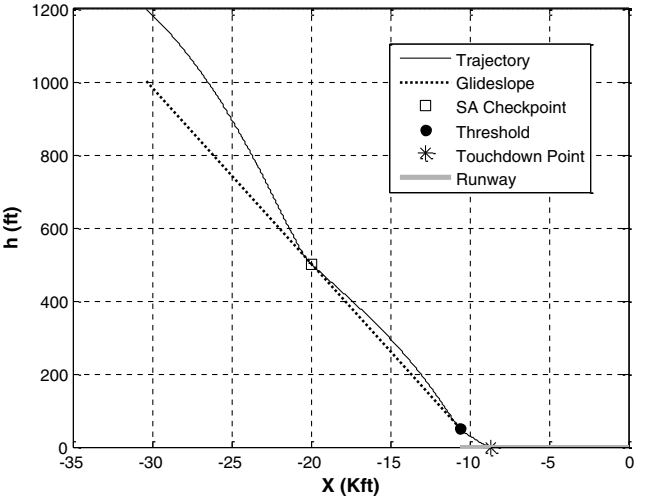

Fig. 4 Landing trajectory in the vertical plane.

B. Landing Under Large Initial Condition Errors

In this landing scenario, the aircraft starts with a lateral error of 500 ft with an initial altitude error of 200 ft from the glideslope at an initial flight path angle of 2.6 deg. Figures 3–5 show the landing trajectories in three dimensions, vertical plane, and horizontal plane,

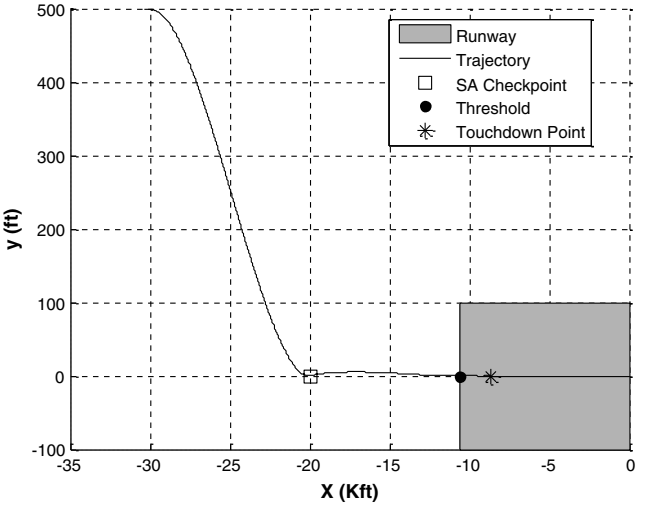

Fig. 5 Landing trajectory in the horizontal plane.

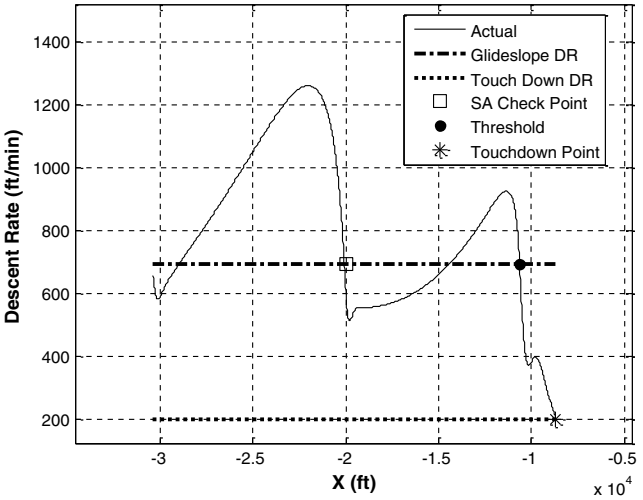

Fig. 6 Descent rates during the stabilized approach and flare.

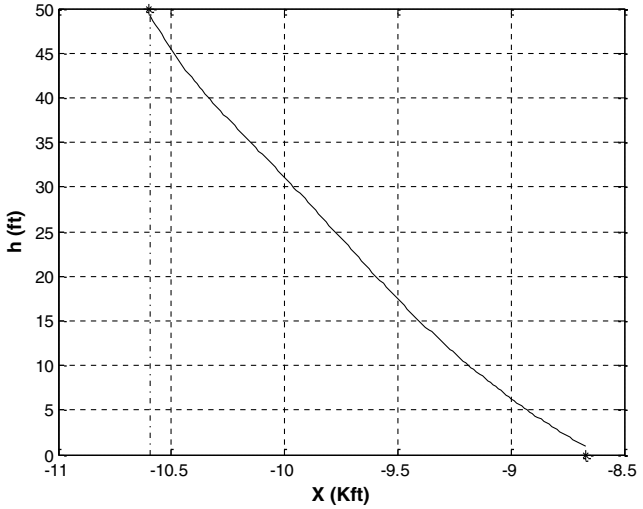

Fig. 7 Trajectory in the vertical plane during the flare maneuver.

respectively. It may be observed that the position errors in the lateral and vertical directions are corrected by the time the aircraft reaches the stabilized approach-check altitude. Thereafter, the aircraft remains very close to the glideslope in the vertical direction and aligned with the runway centerline in the lateral direction. Figure 6 gives the descent rate (DR) of the aircraft. Figures 7 and 8 provide the trajectory in the vertical plane and the descent rate as a function of height above the ground during the flare. Descent rate at touchdown is approximately 197 ft/min, which is within the specified rate of 100 ft/min to 200 ft/min in CFR Part 14.

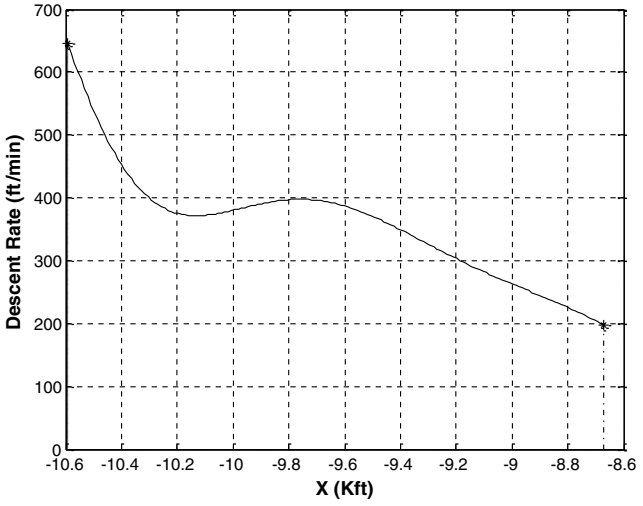

Fig. 8 Descent rate as a function of altitude above the runway during the flare maneuver.

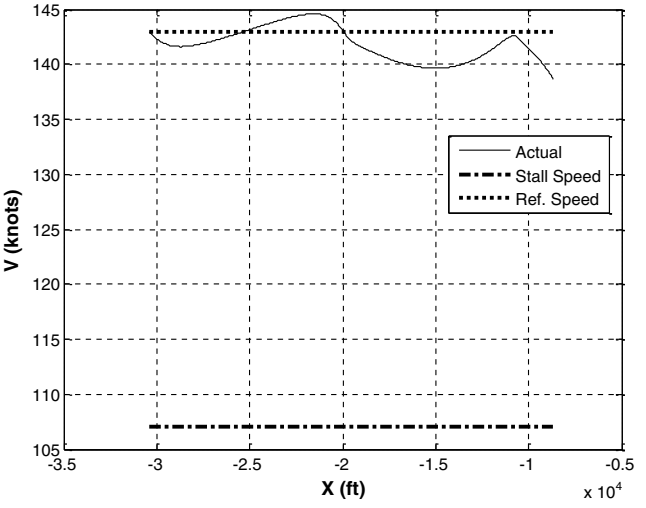

Fig. 9 Airspeed.

Figure 9 shows that the reference airspeed remained within three knots of the specified value throughout the landing trajectory. The commanded and the actual thrust profiles are shown in Fig. 10. The observed thrust transients are due to the tight control tolerances used in the present study. Note that the magnitudes are well within the maximum thrust capacity of 40,000 lbf for the NASA GTM aircraft model.

Figures 11–13 give the commanded and the actual roll, pitch, and yaw attitudes. Commanded and actual values of the roll attitude are zero during the stabilized-approach phase. Following the current operating procedure of using the crabbed approach, the yaw attitude is used to maintain the aircraft on course until the flare maneuver, at which time the roll angle is used to keep the aircraft aligned along the runway centerline. This can be observed in Fig. 11, which shows minor roll gyrations toward the end. Pitch-attitude history shown in Fig. 12 assumes negative values before the aircraft approaches the stabilized approach-check altitude to correct for the 200-ft excess altitude. The pitch-control activity remains small after this stage. The aircraft pitches up by 2 deg to reduce the descent rate during the flare. The yaw-attitude history shown in Fig. 13 exhibits the most activity before the stabilized approach-check altitude is reached. Thereafter,

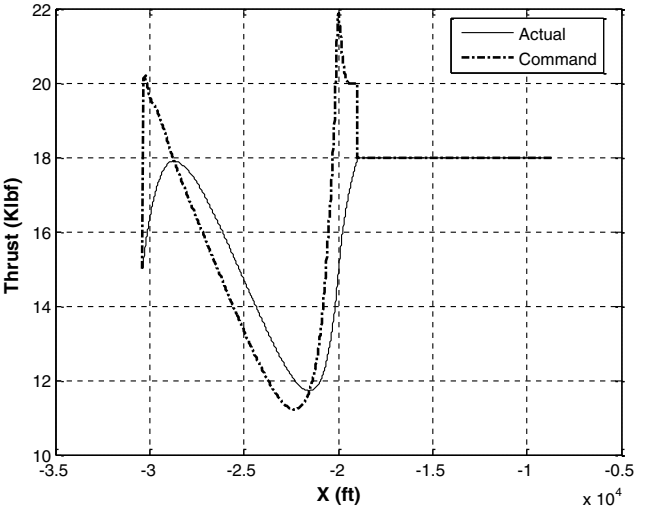

Fig. 10 Commanded and actual thrust.

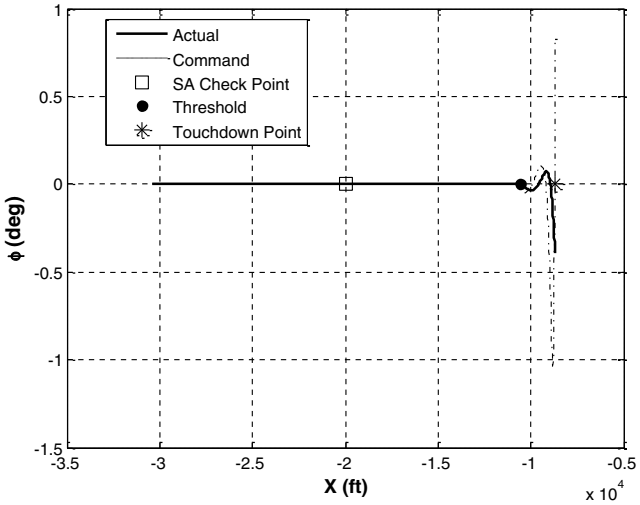

Fig. 11 Actual and commanded roll-attitude histories.

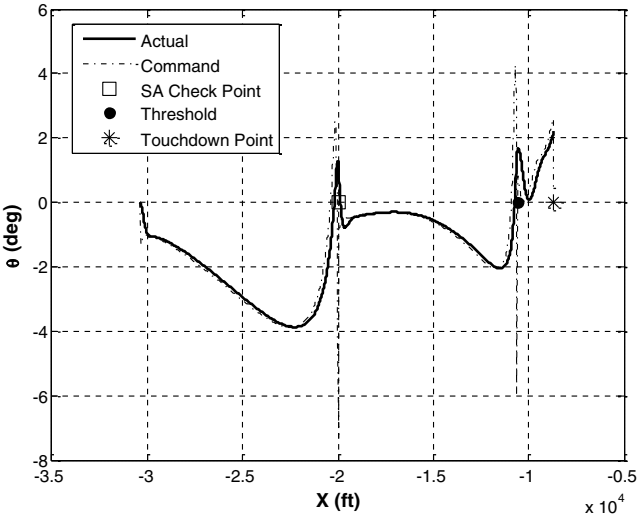

Fig. 12 Actual and commanded pitch-attitude histories.

the aircraft trajectory remains aligned with the runway centerline with very little yaw control activity. The dashed lines in all three plots show the attitude commands generated by the guidance law, and the solid lines indicate the aircraft attitude. The jumps in the commanded values at the waypoints are due to the fact that the control objective

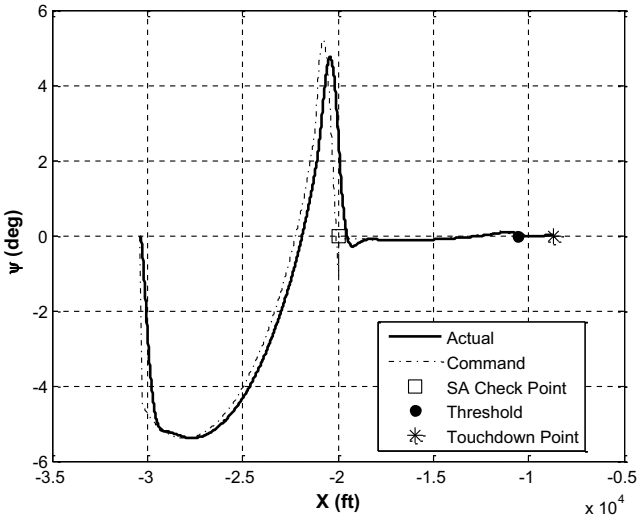

Fig. 13 Actual and commanded yaw-attitude histories.

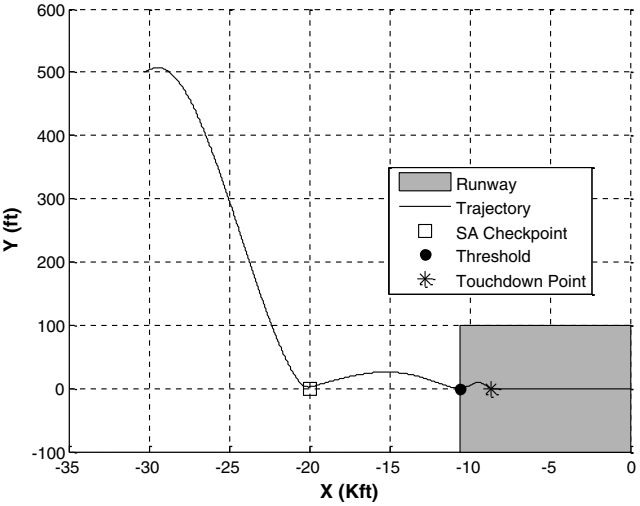

Fig. 14 Landing trajectory in the horizontal plane under 20-knot crosswind.

changes between each waypoint segment and no requirement has been placed on the smoothness of control. If desired, such a requirement can be imposed by introducing additional dynamics at the input. Studies such as these will be of future interest.

C. Landing Under a 20-Knot Crosswind

A 20-kt steady crosswind along the positive *Y* axis is introduced into the simulation to study the response of the guidance law. The landing trajectory in the horizontal plane is shown in Fig. 14. It can be seen in this figure that the aircraft corrects a 500-ft lateral offset in the presence of crosswind by the time it reaches the stabilized approach-check altitude. The pronounced bulge in the trajectory between the stabilized-approach checkpoint and the threshold is due to the combined effect of the crosswind and the airspeed-vector orientation requirement at the waypoint. The specified conditions at the runway threshold and the touchdown point are met by the guidance law. The aircraft lands with a yaw attitude of less than 0.01 deg, a lateral offset of 0.37 ft, and a heading angle of −1.5 deg. Descent rate at touchdown is 218 ft/ min, which is slightly higher than the specified maximum rate, as seen in Fig. 15.

Figures 16 and 17 provide comparisons of the yaw attitude, roll attitude, and angle of sideslip histories under a 20-kt crosswind with those of the nominal landing scenario discussed in the foregoing section. The yaw attitude of the aircraft under crosswind assumes larger values than the nominal landing scenario. This is more

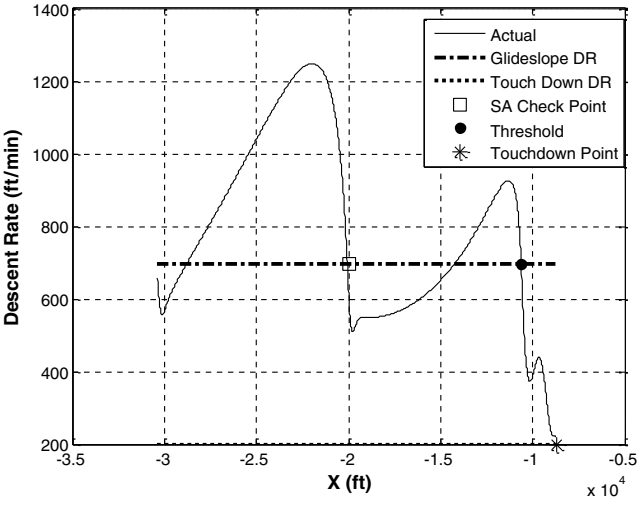

Fig. 15 Descent rate during the stabilized approach and flare under 20-knot crosswind.

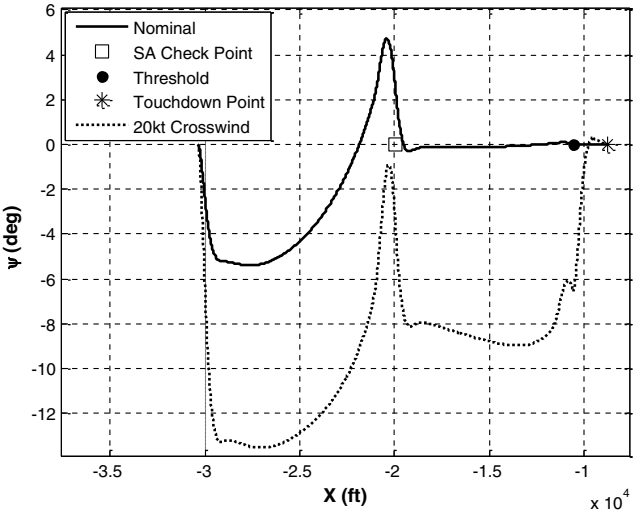

Fig. 16 Yaw-attitude history during the stabilized approach and flare.

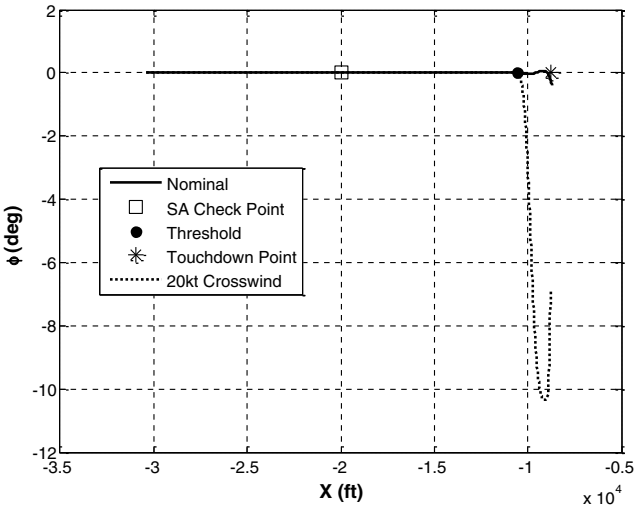

Fig. 18 Roll-attitude history during the stabilized approach and flare.

pronounced in the segment between the stabilized approach-check altitude and the runway threshold, where the yaw attitude assumes a value of approximately 8 deg to tighten the lateral deviation between the aircraft trajectory and the runway centerline in the presence of crosswind. During the decrab maneuver, however, the yaw attitude jumps back to align the nose of the aircraft with the runway, the angle of sideslip develops, and the aircraft banks in the direction of the crosswind, as can be observed in Fig. 18. It should be noted that the aircraft rolls by as much as 10 deg, as opposed to the near-zero values in the nominal-landing scenario.

D. Landing Under 40% Symmetric Reduction of Lift Coefficient

This scenario simulates the loss of lift due to aircraft impairment. The aircraft lift coefficient is reduced by 40% to simulate this case. The landings at 165, 170, and 175 kt are then investigated. Figure 19 gives the vertical plane trajectories at all three speeds, as well as the nominal trajectory at the 142-kt landing speed. All four trajectories are close to one another, indicating that the guidance law was able to accommodate for the reduction in the lift coefficient. This is also confirmed by the descent-rate plots in Fig. 20, where the 40% loss-of-lift coefficient resulted in a vertical speed of approximately 185 ft/s when compared with the 197 ft/s in the nominal scenario. The difference between the two scenarios manifests itself in the angle-of-attack and pitch-attitude histories shown in Figs. 21 and 22, respectively. The aircraft under 40% loss-of-lift coefficient pulls a larger angle of attack and pitch attitude to generate similar lift magnitudes during the flare maneuver. If higher landing speeds are permissible, the maximum angle of attack and pitch attitude will be observed to decrease due to the higher dynamic pressure.

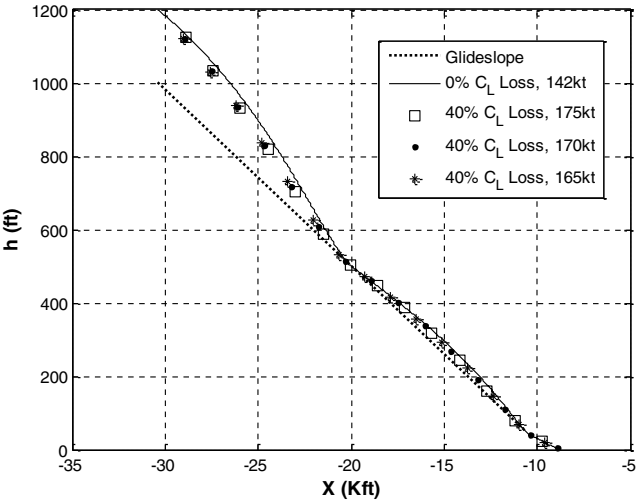

Fig. 19 Vertical-plane trajectories for different landing speeds with 40% loss-of-lift coefficient.

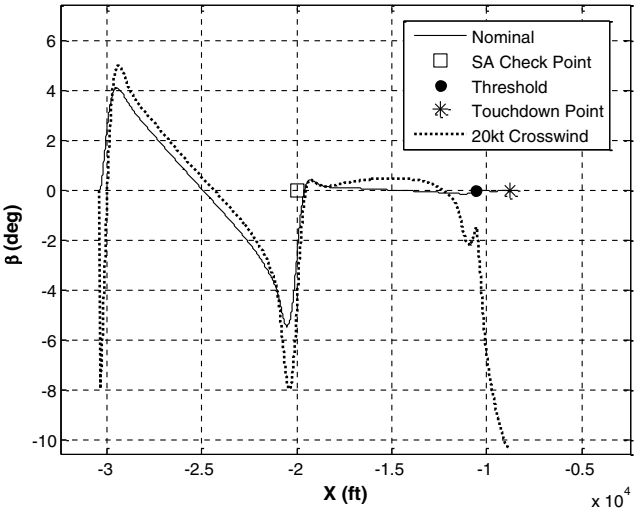

Fig. 17 Angle of sideslip history during the stabilized approach and flare.

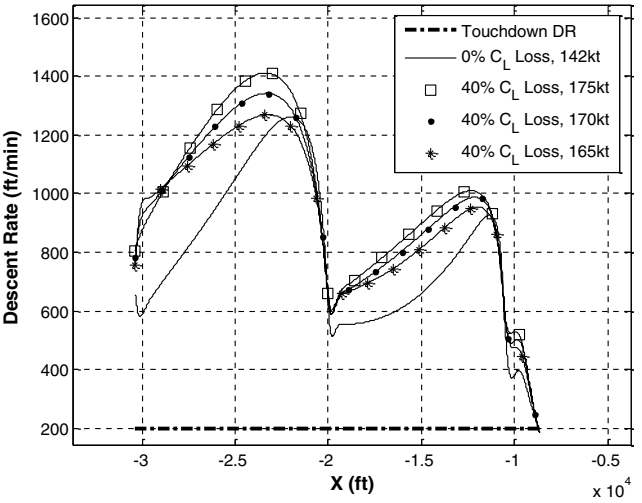

Fig. 20 Descent-rate histories for different landing speeds at 40% loss-of-lift coefficient.

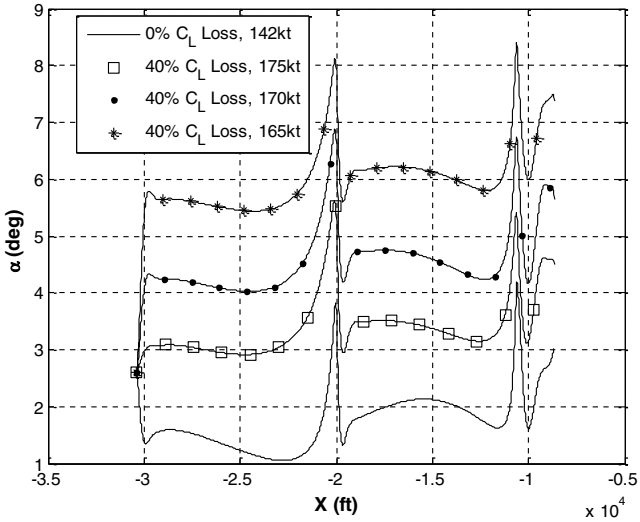

Fig. 21 Angle-of-attack histories for different landing speeds at 40% loss-of-lift coefficient.

The simulation results given in the foregoing sections demonstrate that the guidance system is capable of safely landing normal or impaired aircraft under widely varying operating conditions. The remaining investigations are those of guidance-law robustness and near-optimality, discussed in the following sections.

E. Robustness Evaluation in Monte Carlo Simulations

Because the closed-loop guidance law combined with the aircraft dynamics forms a nonlinear-dynamic system, Monte Carlo simulation methodology can be used to assess the robustness of the system to parameter variations and disturbances.

All uncertainties except the wind gust and ground effect were assumed to be uniformly distributed random numbers. The following uncertainties are included in these simulations:

1) Initial condition errors in altitude measured up to ± 200 ft.

2) Initial lateral offset from the runway measured up to ± 500 ft.

3) Initial heading angle errors of ± 5 deg occurred.

4) Initial flight-path deviations from the glideslope by ± 5 deg were measured.

5) Loss-of-lift coefficient ranged between 35 and 45%.

6) Random wind profiles were generated using the Dryden wind-gust model. Figure 23 shows sample plots of wind components. The initial seed used in generating the band-limited unit variance white-noise signal is set to the Monte Carlo trial number.

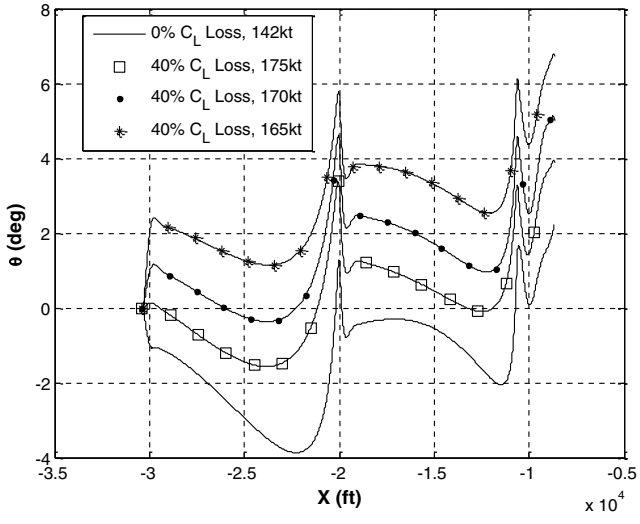

Fig. 22 Pitch-attitude histories for different landing speeds at 40% loss-of-lift coefficient.

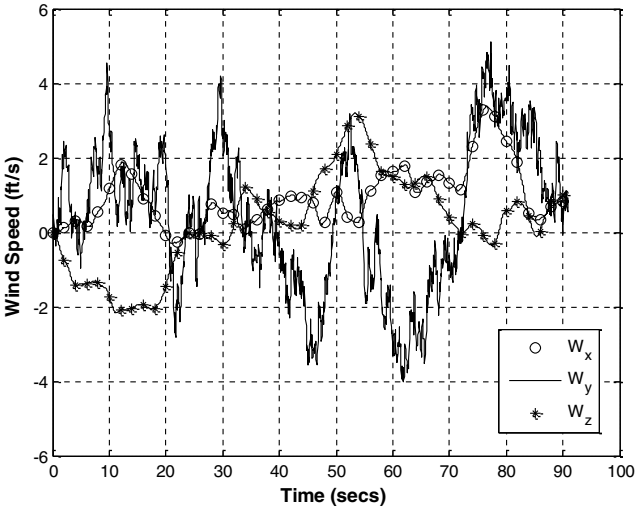

Fig. 23 Wind speeds from Dryden wind-gust model.

7) A ground effect model from Ref. [33] is used in all the Monte Carlo simulation runs.

The performance parameters of interest from the Monte Carlo simulation trials are 1) descent rate at touchdown, 2) lateral offset at touchdown, 3) heading angle at touchdown, and 4) yaw attitude at touchdown. Figure 24 shows the distribution of the descent rates obtained from the 500 Monte Carlo simulation trials. The aircraft makes a positive touchdown (>0 ft/s descent rate) in 93% of the trials. The remaining 7% of the trials result in the ballooning of the trajectory. It is noted that the descent rates at touchdown are lower than the intended 200 ft/min due to the extra lift derived from the ground-effect model. The offset from the centerline at touchdown is less than 5 ft in all the trials, as shown in Fig. 25. The heading angle at touchdown is within ± 1 deg in most trials, as seen in Fig. 26. Finally, Fig. 27 shows that the yaw attitude of the aircraft at touchdown is within ± 0.05 deg.

The Monte Carlo simulation results given in this section demonstrate that the guidance system is robust to system uncertainties and external disturbances within the specified uncertainty bounds.

F. Near Optimality of the Landing-Guidance Law

To examine the optimality of the closed-loop guidance law based on transformed dynamics, a separate numerical trajectory-optimization problem was formulated in the pitch plane. The performance index is chosen as the minimization of the integrated values of the load factor along the vertical-plane trajectory. Note that the closed-loop guidance-law formulation used the integral of the

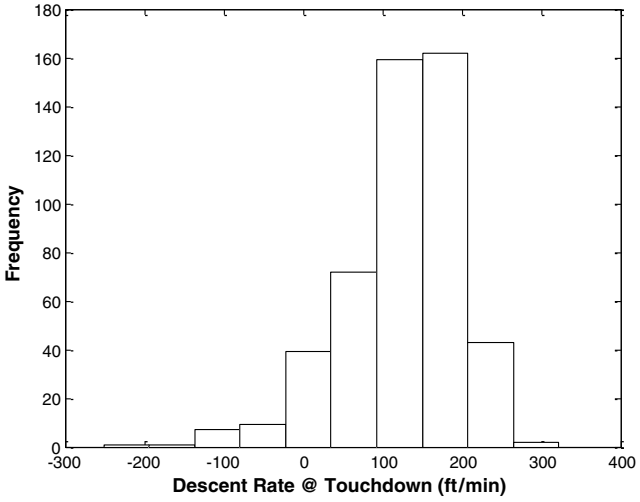

Fig. 24 Distribution of descent rate at touchdown.

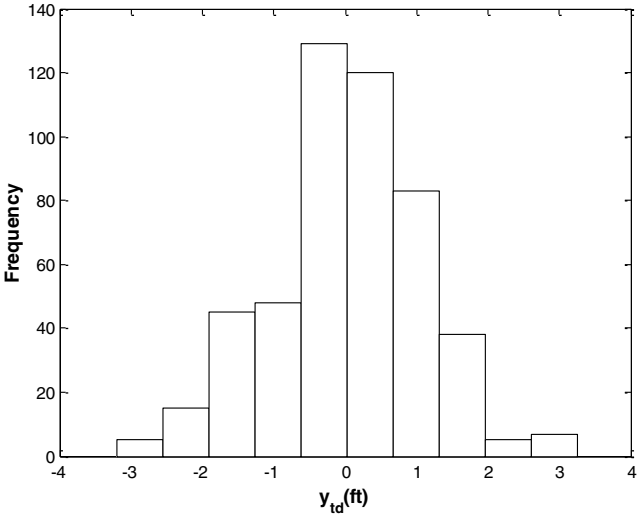

Fig. 25 Distribution of lateral offset at touchdown.

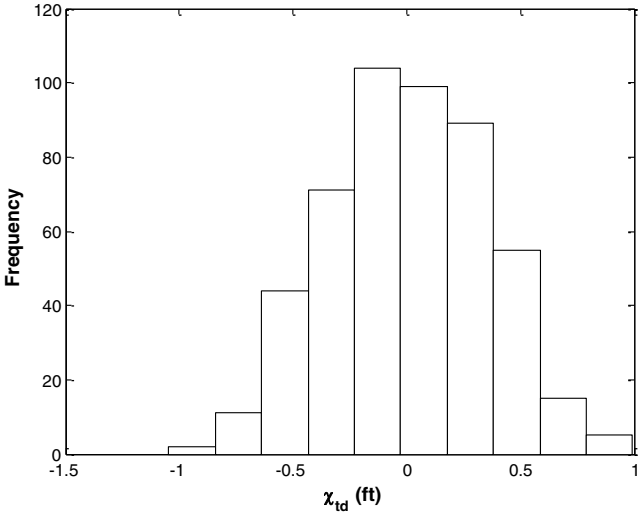

Fig. 26 Distribution of heading angle at touchdown.

vehicle acceleration in the inertial frame. The desired boundary conditions are imposed as constraints in the problem. The pitch-attitude history is approximated by piecewise sixth-order polynomials in time in each of the three landing phases. The

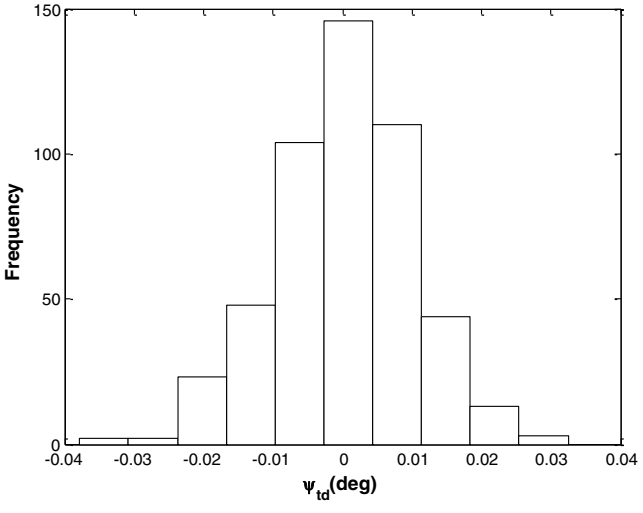

Fig. 27 Distribution of yaw attitude at touchdown.

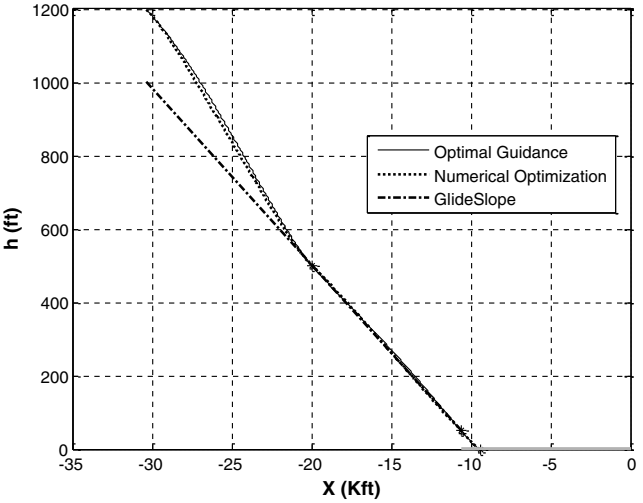

Fig. 28 Comparison between altitude histories during stabilized-approach and flare.

performance index is evaluated by simulating the vertical-plane trajectory using the parameterized pitch-attitude history. The coefficients of the polynomials describing the pitch-attitude history were then chosen by a nonlinear programming algorithm. The MATLAB "fmincon" [34] is used in the present numerical optimization study. The optimization problem does not include the autopilot response to the guidance commands or the response of the engine to the thrust commands. Therefore, these dynamics are removed from the simulation model for the comparisons.

Trajectory and descent rates obtained from numerical optimization compare favorably with those obtained from closed-loop simulations, as shown in Figs. 28–30. Both schemes achieve the desired waypoint conditions, although the intermediate trajectories seem slightly different. Figures 31 and 32 give the pitch-attitude and the angle-of-attack histories. The plots are qualitatively similar in the stabilized-approach segments, differing by less than 1 deg throughout the landing phase. The maximum angle of attack in the flare segment is approximately 3.75 deg, and the maximum pitch attitude is 3 deg, indicating a very small flight-path angle at the time of touchdown.

These numerical optimization results demonstrate the near optimality of the closed-loop guidance law. Minor differences observed may be attributed to the differences in the performance index and the parameterization of the pitch attitude.

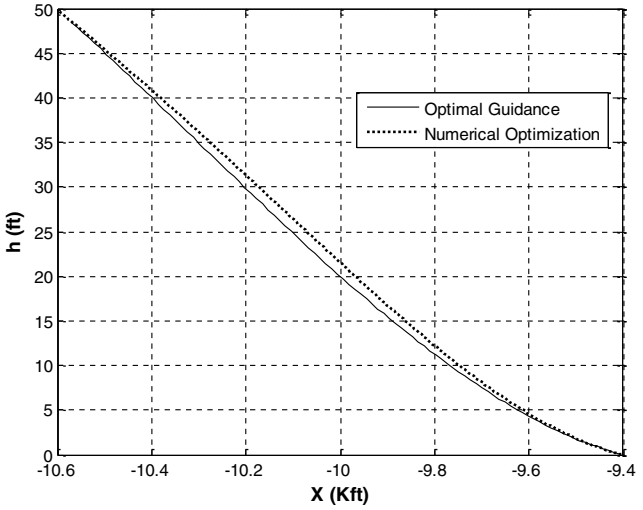

Fig. 29 Comparison between altitude histories during the flare maneuver.

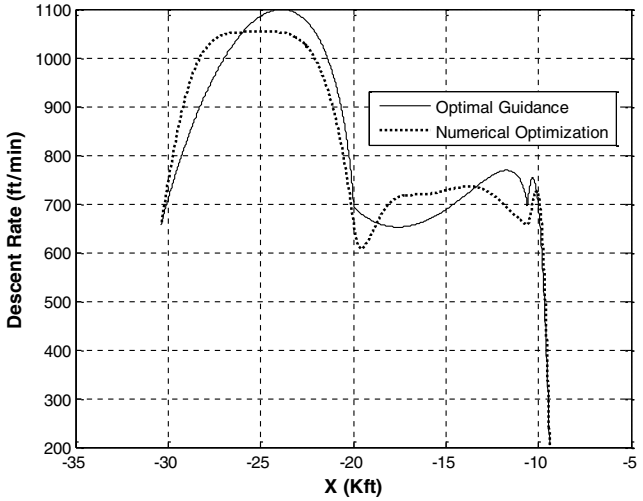

Fig. 30 Comparison between descent rate during stabilized approach and flare.

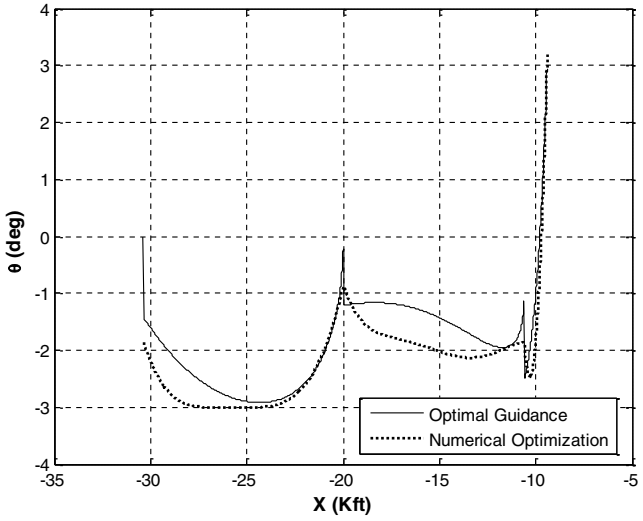

Fig. 31 Comparison between pitch-attitude histories during the stabilized approach and flare.

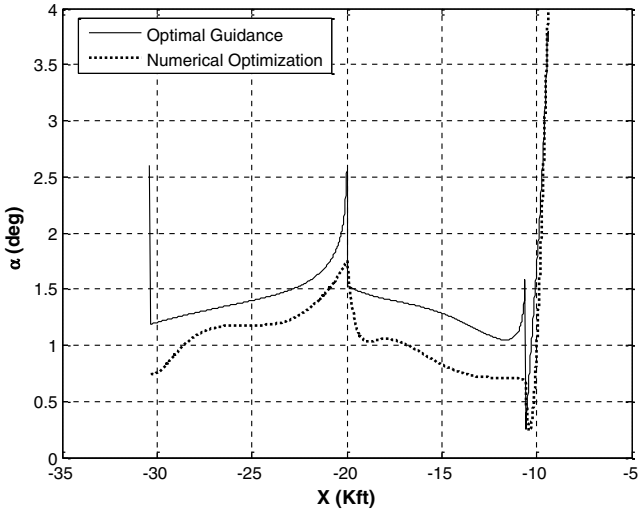

Fig. 32 Comparison between angle-of-attack histories during the stabilized approach and flare.

V. Conclusions

This paper described the development of a landing-guidance law that can be used under normal and impaired conditions. Guidance-law derivation employed a feedback, linearized–nonlinear, point-mass dynamic model of the aircraft. The system dynamics were transformed to a linear, time-invariant, decoupled form using differential geometric transformation. Differential-game theory was then employed to synthesize the guidance law. Inverse transformation of the guidance law then produced a nonlinear, time-varying, coupled guidance law. Specialization of the guidance law for bank-to-turn and skid-to-turn maneuvers was illustrated. Performances of the guidance law under both normal and impaired aircraft conditions were then demonstrated. Robustness of the guidance law to a class of disturbances such as crosswind, wind gust, aerodynamic model uncertainties, and ground effect was demonstrated in Monte Carlo simulations. Finally, the guidance-law performance was compared with a numerically optimized trajectory to verify the near optimality of the proposed approach. Evaluation of this guidance law in manned simulations will be of future interest.

The following conclusions can be drawn based on the present research:

1) The present work demonstrated that it is feasible to develop guidance laws for executing complex flight maneuvers required for landing impaired aircraft.

2) The guidance law must be made robust with respect to aircraft model and environmental uncertainties. This paper showed that the required robustness can be achieved using the theory of differential games.

3) The proposed analytical approach has been shown to be near optimal by comparing the results with a nonlinear programming-based numerical trajectory optimization.

The computations required for implementing the guidance law are modest enough to permit its integration with existing flight-control systems on board modern transport aircraft.

Acknowledgments

This research was supported under NASA Contract number NNX09CC01P, with John Kaneshige as the Technical Monitor. The authors would like to thank John Kaneshige, K. Krishnakumar, and Nhan Nguyen of NASA Ames Research Center for their support and enthusiasm for this research. Vivian Lin of Optimal Synthesis, Inc., developed the data interface with FlightGear simulation program to create the animations used in evaluating the simulation results.

References

[1] Nguyen, N., Krishnakumar, K., Kaneshige, J., and Nespeca, P., "Dynamics and Adaptive Control for Stability Recovery of Damaged Asymmetric Aircraft," *AIAA Guidance, Navigation, and Control Conference and Exhibit*, AIAA Paper 2006-6049, Keystone, Colorado, Aug. 21–24, 2006.

[2] Nguyen, N., Krishnakumar, K., Kaneshige, J., and Nespeca, P., "Flight Dynamics and Hybrid Adaptive Control of Damaged Aircraft," *Journal of Guidance, Control, and Dynamics*, Vol. 31, No. 3, May–June 2008, pp. 751–764. doi:10.2514/1.28142

[3] Rysdyk, R. T., and Calise, A. J., "Fault-Tolerant Flight Control via Adaptive Neural Network Augmentation," AIAA Paper 1998-4483, 1998.

[4] Tandale, M. D., and Valasek, J., "Fault-Tolerant Structured Adaptive Model Inversion Control," *Journal of Guidance, Control, and Dynamics*, Vol. 29, No. 3, May–June, 2006, pp. 635–642. doi:10.2514/1.15244

[5] Anon., "Airplane Flying Handbook", FAA Document No. H-8083-3A, U.S. Department of Transportation: Federal Aviation Administration, Washington, DC, 2004.

[6] Kim, J., Palaniappan, K., and Menon, P. K., "Rapid Estimation of Impaired Aircraft Aerodynamic Parameters Aircraft Performance Models using Differential Vortex Panel Method and Extended Kalman Filter," *Journal of Aircraft*, Vol. 47, No. 4, July–Aug. 2010, pp. 1216–1228.

doi:10.2514/1.46914
[7] Anon., *Code of Federal Regulations: Part 14, Aeronautics and Space, Parts 1 to 50*, U.S. Government Printing Office, Washington, DC, Jan. 2007.
[8] McLean, D., *Automatic Flight Control Systems*, Prentice Hall, New York, 1990, pp. 401–404.
[9] McRuer, D., Ashkenas, I., and Graham, D., *Aircraft Flight Dynamics and Automatic Control*, Princeton Univ. Press, Princeton, NJ, 1973, pp. 623–660.
[10] Jorgensen, C. C., and Schley, C., "A Neural Network Baseline Problem for Control of Aircraft Flare and Touchdown," *Neural Networks for Control*, edited by W. T. Miller III, R. S. Sutton, and P. J. Werbos, The MIT Press, Cambridge, MA, 1990.
[11] Schaefer, D. R., "Functional Development of the 757/767 Digital CAT IIIB Autoland System," AIAA Paper 83-2192, Aug. 1983.
[12] Shakarian, A., "Application of Monte-Carlo Techniques to the 757/767 Autoland Dispersion Analysis by Simulation," AIAA Paper 83-2193, Aug. 1983.
[13] Wagner, T., and Valasek, J., "Digital Autoland Control Laws Using Quantitative Feedback Theory and Direct Digital Design," *Journal of Guidance, Control, and Dynamics*, Vol. 30, No. 5, Sept.–Oct. 2007, pp. 1399–1413.
doi:10.2514/1.27761
[14] Shue, S.-P., Agarwal, R. K., and Shi, P., "Robust Aircraft Control Design for Glideslope Capture in Windshear Using Gain Scheduling," AIAA Paper 98-4299, Aug. 10–12, 1998.
[15] Nho, K., and Agarwal, R. K., "Glideslope Capture in Wind Gust via Fuzzy Logic Controller," AIAA Paper 1999-635, Jan. 1999.
[16] Nho, K., and Agarwal, R. K., "Automatic Landing System Design Using Fuzzy Logic," *Journal of Guidance, Control, and Dynamics*, Vol. 23, No. 2, 2000, pp. 298–304.
doi:10.2514/2.4522
[17] Heffley, R. K., "Closed-Loop Analysis of Manual Flare and Landing," *Journal of Aircraft*, Vol. 13, No. 1, Feb. 1976, pp. 83–88.
[18] Arents, R. R. D., Groeneweg, J., Mulder, M., and van Paassen, M. M., "Predictive Landing Guidance in Synthetic Vision Displays," AIAA Paper 2009-5984, Aug. 2009.
[19] Ngoc, L. L., Borst, C., Mulder, M., and van Paassen, M. M., "The Effect of Synthetic Vision Enhancements on Landing Flare Performance," AIAA Paper 2010-8170, Aug. 2010.
[20] Prasad, B., and Pradeep, S., "Automatic Landing System Design Using Feedback Linearization Method," AIAA Paper 2007-2733, May 2007.
[21] Kluver, C. A., "Unpowered Approach and Landing Guidance Using Trajectory Planning," *Journal of Guidance, Control, and Dynamics*, Vol. 27, No. 6, Nov.–Dec. 2004, pp. 967–974.
doi:10.2514/1.7877
[22] Kluver, C. A., "Unpowered Approach and Landing Guidance with Normal Acceleration Limitations," *Journal of Guidance, Control, and Dynamics*, Vol. 30, No. 3, May–June 2007, pp. 882–885.
doi:10.2514/1.28081
[23] Kim, D., Choi, Y., and Suk, J., "A Glidepath Tracking Algorithm for Autolanding of a UAV," AIAA Paper 2005-6979, Sept. 2005.
[24] Bryson, A. E., and Ho, Y. C., *Applied Optimal Control*, Hemisphere, New York, 1975.
[25] Issacs, R., *Differential Games*, Robert E. Krieger Publishing Company, Huntington, NY, 1975.
[26] Menon, P. K., "Short-Range Nonlinear Feedback Strategies for Aircraft Pursuit-Evasion," *Journal of Guidance, Control, and Dynamics*, Vol. 12, Jan.–Feb. 1989, pp. 27–32.
doi:10.2514/3.20364
[27] Menon, P. K., and Duke, E. L., "Time-Optimal Aircraft Pursuit-Evasion with a Weapon Envelope Constraint," *Journal of Guidance, Control, and Dynamics*, Vol. 15, No. 2, March–April 1992, pp. 448–456.
doi:10.2514/3.20856
[28] Menon, P. K., and Calise, A. J., "Interception, Evasion, Rendezvous, and Velocity-to-be-Gained Guidance for Spacecraft," AIAA Paper 1987-2318, Aug. 1987.
[29] Menon, P. K., "Aerobrake Guidance Law Synthesis Using Feedback Linearization," *1991 American Control Conference*, Boston, June 26–28, 1991.
[30] Kreyszig, E., *Differential Geometry*, Dover, New York, 1991.
[31] Isidori, A., *Nonlinear Control Systems*, Springer–Verlag, New York, 1985.
[32] Marino, R., and Tomei, P., *Nonlinear Control Design*, Prentice Hall, New York, 1995.
[33] "FLTz Aircraft Simulation Software Version 4.2", NASA Technical Point of Contact: John Kaneshige, Code TI, NASA Ames Research Center, Mail Stop: 269-1, Moffet Field, CA, 94035-1000, Feb. 2009.
[34] Anon, *Optimization Toolbox for MATLAB®*, The MathWorks, Inc., Natick, MA, 2007.

J. Valasek
Associate Editor